Materials Transactions, Vol. 59, No. 1 (2018) pp. 110 to 116

Influence of Cooling Rate on Primary Particle and Solute Distribution in High-Speed Twin-Roll Cast Al-Mn Based Alloy Strip

Ram Song*, Yohei Harada and Shinji Kumai

Department of Materials Science and Engineering, Tokyo Institute of Technology, Tokyo 152–8552, Japan

Binary Al-Mn, ternary Al-Mn-Fe and Al-Mn-Si alloys were prepared by different cooling rates during solidification using direct chill-casting and high-speed twin-roll casting. Mn concentration and solute distribution in Al matrix were examined. The Mn concentration in solid solution was considered almost equivalent in as-cast condition. In contrast, much amount of decomposition of supersaturated Mn in solid solution occurred in high-speed twin-roll cast alloys after homogenization. In high-speed twin-roll cast strips, fine distribution of constituent particles in Al-Mn-Fe alloy and homogeneous solute distribution in Al matrix in Al-Mn-Si alloy were obtained due to the high cooling rate of the high-speed twin-roll casting. After homogenization treatment, coarsening and spheroidization of the constituent particles were mainly observed in Al-Mn-Fe alloy, while formation of fine dispersoids was predominantly observed in Al-Mn-Si alloy. Such differences in microstructure resulted from the decomposition behavior of supersaturated Mn in solid solution. [doi:10.2320/matertrans.F-M2017843]

(Received August 8, 2017; Accepted October 6, 2017; Published November 17, 2017)

Keywords: *high-speed twin-roll casting, cooling rate, solute distribution, aluminum-manganese-iron alloy, aluminum-manganese-silicon alloy*

1. Introduction

In wrought Al-Mn based alloys, the Mn alloying element can be solid-dissolved in the Al matrix and also form Mn-containing constituent particles. The supersaturated Mn precipitates to form fine dispersoids during heat treatment. The second-phase particles including constituent particles and fine dispersoids have significant roles to determine various metallurgical characteristics in wrought Al-Mn based alloys; recrystallization behavior and final mechanical properties[1–8]. For instance, well distributed constituent particles, mainly formed during solidification, can act as nucleation site of recrystalized grains in annealing process[3,4]. Also, fine dispersoids, mainly formed by decomposition of supersaturated Mn in solid solution during heat treatment, can pin the grain boundary movement and thus inhibit recrystallization[5,6]. The formation of fine dispersoids are influenced by other alloying elements as well as Mn solubility in Al matrix. The level of Mn concentration in Al matrix and formation of constituent particles and its distribution in wrought Al-Mn based alloys are strongly influenced by cooling rates of the starting cast alloys.

Recently, high-speed twin-roll casting (HSTRC) has attracted attention as a casting procedure for producing aluminum strip with high productivity[9–16]. The HSTRC can fabricate thin aluminum alloy strips from the melt, directly. Also, extremely high cooling rate can be achieved, in particular at the near-surface area of strip. This feature contributes to get high solid solubility in matrix and homogeneous distribution of primary particles. The effect of high cooling rate was confirmed in several kinds of aluminum alloy strips; refined primary aluminum dendrite- and eutectic solidified structure[10], morphological change of second-phase particle[15]. For wrought Al-Mn based alloys, the HSTRC can lead to Mn supersaturation and refined primary particles as well as its homogeneous distribution. Therefore, the HSTRC is superior to control the final microstructure and mechanical properties of wrought Al-Mn based alloys compared to that of other conventional manufacturing processes like direct chill (DC)-casting.

In the present study, Al-Mn based alloy strips were fabricated by HSTRC. To demonstrate the effect of cooling rate on solute distribution, HSTRC strip was compared to conventional DC-cast samples, and constituent particle distribution and solute concentration in Al matrix were investigated. The decomposition behavior of supersaturated Mn in high-speed twin-roll cast alloys was discussed.

2. Experimental Procedure

Three kinds of Al-Mn based alloys were prepared. They were binary Al-Mn, ternary Al-Mn-Fe and Al-Mn-Si alloys, which are referred as AM, AMF and AMS, respectively. Their chemical compositions are shown in Table 1. DC-cast billets (60 mm wide × 190 mm long) were produced by Mitsubishi Aluminum Co., Ltd. Some of them were re-melted, then cast by HSTRC. Figure 1 illustrates a schematic of high-speed twin-roll caster. The diameter and width of pure copper rolls were 300 mm and 100 mm, respectively. The rolls were cooled by running water to prevent increasing roll temperature during the casting. One of the rolls was fixed, firmly on the base, while the other roll was installed with a series of springs for controlling the initial roll seperation force as 20–60 kN. The roll rotating speed was 60 m/min. The contact length between the melt and roll surface was about 100 mm. The initial roll gap was set as 1 mm. The

Table 1 Chemical compositions of the alloys. (in mass%)

*Alloy	Mn	Fe	Si	other	Al
AM	1.190	0.001	0.001	0.002	Bal.
AMF	1.190	0.970	0.002	0.001	Bal.
AMS	1.130	0.003	0.920	0.002	Bal.

Note: AM, AMF and AMS are corresponded to Al-Mn binary, Al-Mn-Fe and Al-Mn-Si ternary alloy, respectively.

*Graduate Student, Tokyo Institute of Technology. Corresponding author, E-mail: song.r.aa@m.titech.ac.jp

HSTRC procedure is as follows; About 2.5 kg molten alloy was poured into the nozzle. The melt was solidified on the both roll surfaces, to form solidification shells. The solidified shells encountered at the roll gap by roll rotation, and rapidly cooled. At last, the solidifying alloy passed through the roll gap to produce a thin strip. The cast strip was around 3 m-long and 100 mm-wide. The middle part of around 1 m in resultant strip was stable thickness along the casting direction, which is around 2.2 mm for AM and AMF, and around 2.6 mm for AMS, respectively.

During the HSTRC, temperature change was measured by ultra-thin foil thermocouples (40 μm in thickness, AMBE SMT Co.). The data was recorded by data logger (KEYENCE, NR600) in 500 ms interval. The measured points were surface and center area of the strip. After the casting, homogenization treatment (HOMO) was conducted in a salt bath at 450°C for 8 h. The samples were quenched into water after the heat treatment. The electrical conductivity was measured at room temperature by using SIGMA tester with 500 kHz probe (AutoSigma 3000, GE Inspection Technology) to estimate supersaturated Mn content in solid solution. EPMA (JXA-8200, JEOL) analysis by wavelength-dispersive spectrometer (WDS) was performed to investigate the chemical composition ratio of primary particles and the solute distribution in Al matrix. The accelerating voltage and beam current were set to 15 kV and 2×10^{-7} A, respectively.

It should be mentioned that specimens for microstructure observation were collected from the HSTRC strip where the strip thickness was constant. Also, the electrical conductivity measurement and composition analysis were carried out on the normal-direction plane and casting-direction plane of the HSTRC strip, respectively. Meanwhile, the DC-cast samples were collected from the mid-central area of the DC-cast billet representing the low cooling rate during solidification. In present study, the cooling rate of DC-cast billet was estimated less than 10^1 K/s.

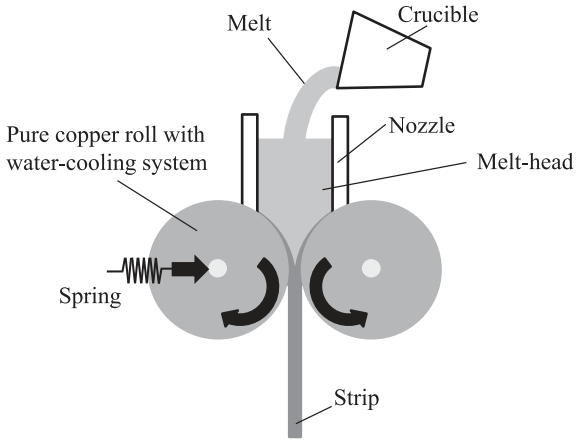

Fig. 1 Schematic of the high-speed twin-roll caster.

3. Results and Discussions

3.1 Temperature profile during HSTRC

Figure 2 shows the temperature profile obtained by direct measurement during HSTRC. The change in position of the thermocouple during HSTRC is also shown as (a) to (d) in Fig. 2. When a thermocouple was inserted from under the nozzle into surface area of the strip, the temperature increased as marked by (a). Following the roll rotation, the thermocouple trapped by growing solidified shell, was pulled into the roll gap. At the passing through the roll gap, the temperature drastically decreased as marked by (b) due to the heat was transferred very rapidly through the solid shells contacting to the casting rolls. Submerging another thermocouple into the melt-head inside of the feeding nozzle, the temperature showed quite constant value as marked by (c). Once the thermocouple was caught by the solidification shells growing from both roll surfaces, the temperature decreased dramatically as marked by (d). From the cooling curve during HSTRC, it was revealed that the cooling rate was over 10^3 K/s even at the strip center as well as surface area.

3.2 Electrical conductivity change after HOMO

The electrical conductivity of Al alloy is in inverse relationship to the concentrations of solute elemenets in solid solution[17]. As increasing the concentration of solute elements in the solid solution, the electrical conductivity decreases. In general, the electrical conductivity can be expressed to electrical resistivity value by the eq. (1):

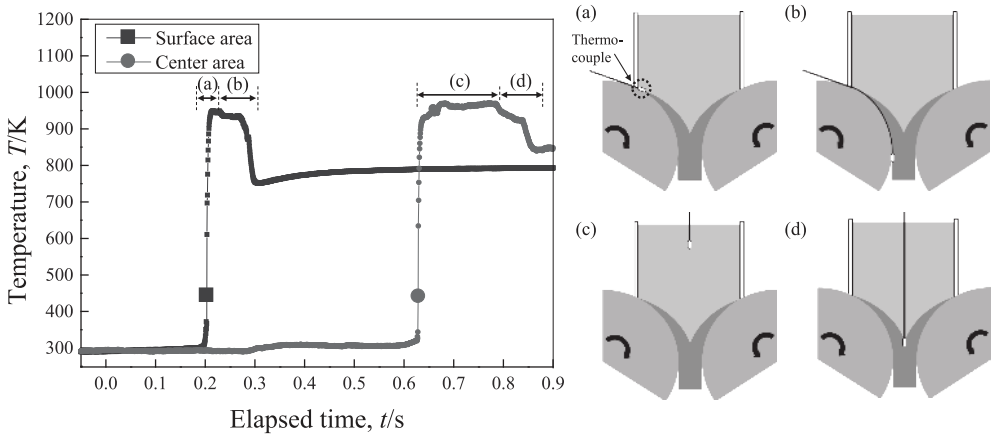

Fig. 2 Temperature profile on each position of the strip during HSTRC.

$$1724.1/\%\text{IACS} = \rho/\text{n}\Omega\text{m} \quad (1)$$

In AM, variation of Mn in solid solution mainly affects its electrical conductivity. For other alloying elements as Fe and Si in the present study, the solubility of Fe in Al matrix is quite low[18], and it is considered that Si in solid solution has much less influence on electrical conductivity than Mn[8]. Therefore, the change of electrical conductivity in AMF and AMS is also considered to be mainly due to the variation of Mn in solid solution. From the electrical conductivity measurement, the Mn concentration in solid solution can be estimated by:

$$\text{Mn(mass\%)} = (\rho_{\text{measure}} - \rho_{\text{pure Al}})/\Delta\rho_{\text{Mn in Al alloy}} \quad (2)$$

where, ρ_{measure} is the electrical resistivity of alloy converted by measured electrical conductivity, $\rho_{\text{pure Al}}$ is the electrical resistivity of pure aluminum, which is 26.5 nΩm at room temperature[19], and $\rho_{\text{Mn in Al alloy}}$ is the electrical resistivity contribution for Mn solute atom in Al matrix. The value of $\Delta\rho_{\text{Mn in Al alloy}}$ is 31 nΩm mass%$^{-1}$ at room temperature[19]. Table 2 shows electrical conductivity change and the estimated Mn concentration in solid solution on both samples of DC-cast and HSTRC strip. The electrical conductivity in as-cast condition showed almost equivalent value in spite of different cooling rate. It means the concentration of Mn in solid solution is almost the same in as-cast condition. In contrast, after HOMO, the electrical conductivity change was dependent on each alloy with different casting method. For AM, no specific change was observed after HOMO in electrical conductivity. This indicates the decomposition of supersaturated solid solution hardly occurred during HOMO. Kolby *et al.*[20] and Haan *et al.*[21] also reported that the Mn precipitation is sluggish in high-purity Al-Mn binary alloy. In contrast to AM, AMF and AMS showed the apparent increase of electrical conductivity after HOMO. It is because the addition of Fe or Si in Al-Mn based alloy promotes the decomposition of supersaturated Mn in solid solution during heat treatment by formation of Mn-containing secondary phases such as orthorhombic Al_6(Mn,Fe) or cubic α-phase[6,20–22]. Moreover, the change of electrical conductivity was dependent on the casting methods, representing different cooling rate during solidification. HSTRC strip showed much amount of decomposition of supersaturated Mn in solid solution in sipte of the equivalent value of Mn concentration in as-cast condition at same alloy system. This suggests that cooling rate has influence on the decomposition behavior of supersaturated Mn content during HOMO.

3.3 Difference in second-phase particle distribution after HOMO

The optical micrographs of microstructure of DC-cast sample and as-cast HSTRC strip are shown in Fig. 3. The distribution of constituent particles can be observed by etched pits. Note that it was hard to observe any second-phase particle in AM. Basically, AMF showed relatively high-dense constituent particles compare to AMS for both casting method. This is considered to result from low Fe solubility in Al matrix. A relatively coarse primary and eutectic constituent particles were observed in DC-cast AMF. In DC-cast AMS, the constituent particles were observed at the grain boundaries and within Al grains. In case of HSTRC strip, the constituent particles were much finer than DC-cast sample, and were located along the cell/grain boundaries. The particles were randomly distributed inside of Al grains as shown in Fig. 3 (c) and (d). The microstructure of DC-cast and HSTRC strip after HOMO of each alloys is also

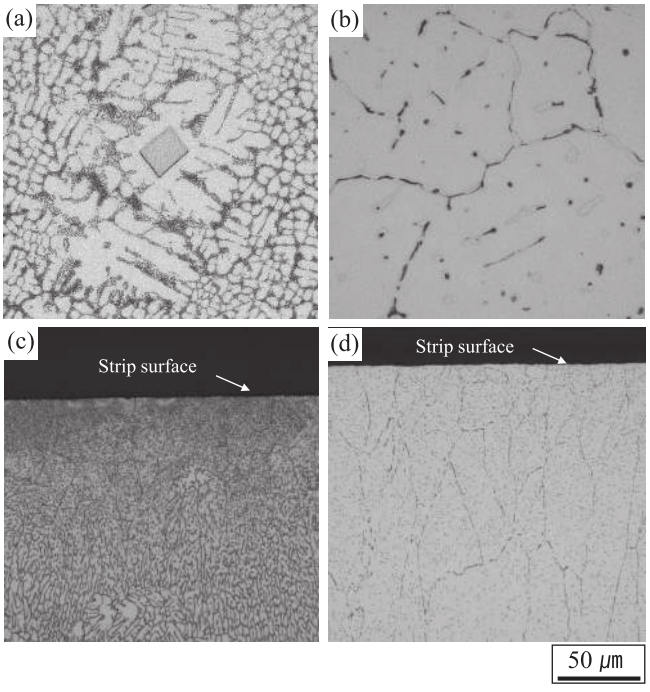

Fig. 3 Microstructure of as-cast DC-cast sample and HSTRC strip. (a) DC-cast AMF, (b) DC-cast AMS, (c) HSTRC strip AMF, (d) HSTRC strip AMS.

Table 2 Electrical conductivity and its corresponding estimation of Mn in solid solution.

Alloy	Casting method	Electrical conductivity (%IACS)		Estimated Mn concentration in solid solution (mass%)	
		As-cast	As-HOMO	As-cast	As-HOMO
AM	DC-casting	26.96	27.00	1.21	1.21
	HSTRC	26.78	27.35	1.22	1.18
AMF	DC-casting	30.82	36.35	0.95	0.68
	HSTRC	30.58	41.48	0.96	0.49
AMS	DC-casting	27.51	43.26	1.17	0.43
	HSTRC	27.68	48.29	1.15	0.30

shown in Fig. 4. Compared to Fig. 3 and Fig. 4, for the AMF after HOMO, there was no specific difference in optical microstructural appearance both DC-cast sample and HSTRC strip. However, AMS exhibited a clear change in evolution of secondary particles after HOMO by the casting method. Most of dispersoids were observed at periphery of the primary α-Al dendrite in AMS DC-cast. Judging from the etch-pits of the dispersoids, shape of the primary α-Al dendrite was clearly revealed as shown in Fig. 4 (b). In contrast, high-dense of dispersoids were observed inside of α-Al grains homogeneously in HSTRC strip after HOMO (in Fig. 4 (d)). Etch-pit free regions were only observed near the cell/grain boundaries. These dispersoids evolution after HOMO is considered to be strongly correlated with the solute distribution in Al matrix during solidification.

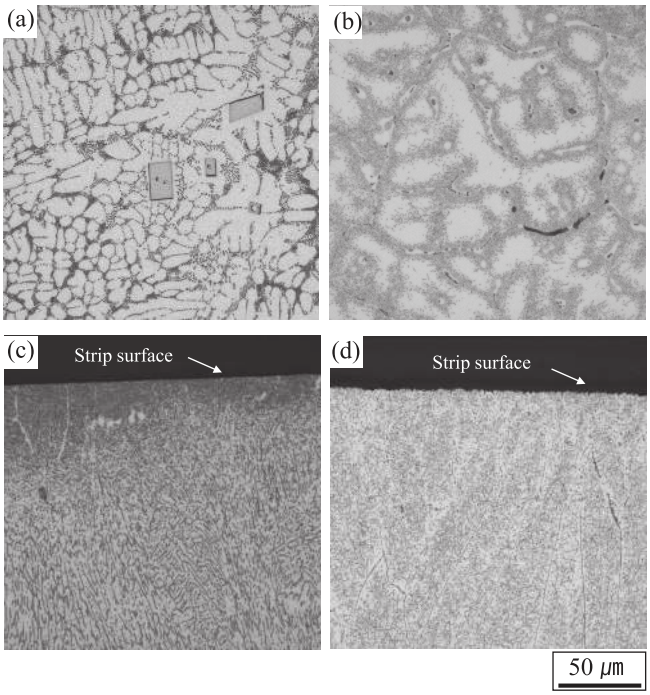

Fig. 4 Microstructure of as-HOMO DC-cast sample and HSTRC strip. (a) DC-cast AMF, (b) DC-cast AMS, (c) HSTRC strip AMF, (d) HSTRC strip AMS.

3.4 Solute distribution in Al matrix and supersaturated Mn decomposition behavior

3.4.1 Al-Mn-Fe ternary alloy

Figure 5 shows the EPMA results of AMF for DC-cast sample and HSTRC strip as-cast condition with a color bar indicating atomic concentration. The area subjected for EPMA analysis was marked by dotted line as shown in Fig. 5 (a) and (b). Due to the low Fe solubility in Al, the matrix was displayed black color in Fe mapping as shown in Fig. 5 (d). Both Mn-rich and Fe-rich areas are corresponded to constituent particle, which is Al_6(Mn,Fe) phase. This constituent particle was much finer and homogeneously distributed in HSTRC strip resulting from the high cooling rate of HSTRC compared to DC-cast. Due to the high cooling rate at HSTRC strip surface, relatively higher Mn concentration in Al matrix was observed (Fig. 5 (e)). However, the Fe was not solid-dissolved in Al matrix as shown in Fig. 5 (f).

In order to examine the evolution of constituent particle and fine dispersoids in detail during HOMO, the microstructure including particle distribution was observed using FE-SEM back-scattered technique as shown in Fig. 6. Due to the high cooling rate in HSTRC strip, much finer primary α-Al dendrite is observed compared to DC-cast sample (see Fig. 5 (a) and (b)). Likewise, the constituent particle size is also certainly finer in HSTRC strip. It can be seen the eutectic with fine lamellar structure in DC-cast as shown in Fig. 6 (a). Inside of α-Al, other primary particles were not observed in as-cast condition. In contrast, some fine dispersoids were observed inside of α-Al at some local regions in as-HOMO condition as shown in Fig. 6 (b). Moreover, the eutectic particles were spheroidized and coarsened. This

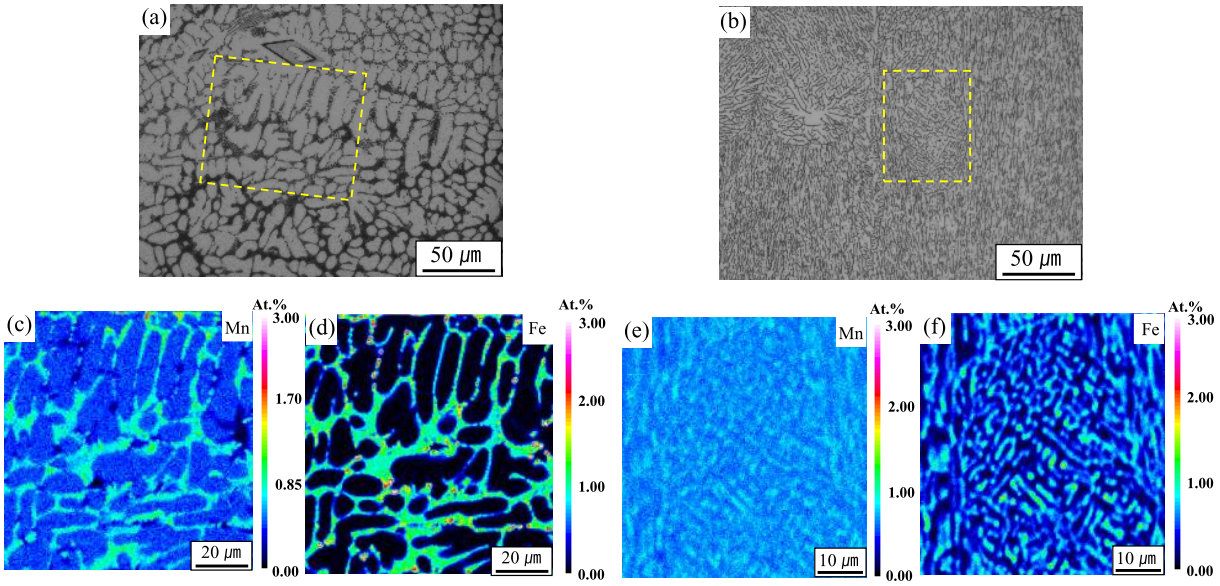

Fig. 5 Solute distribution in Al-Mn-Fe alloy. Locations where the EPMA analysis was performed in (a) DC-cast, and (b) HSTRC strip. Element mapping results of (c) Mn in DC-cast, (d) Fe in DC-cast, (e) Mn in HSTRC strip, (f) Fe in HSTRC strip.

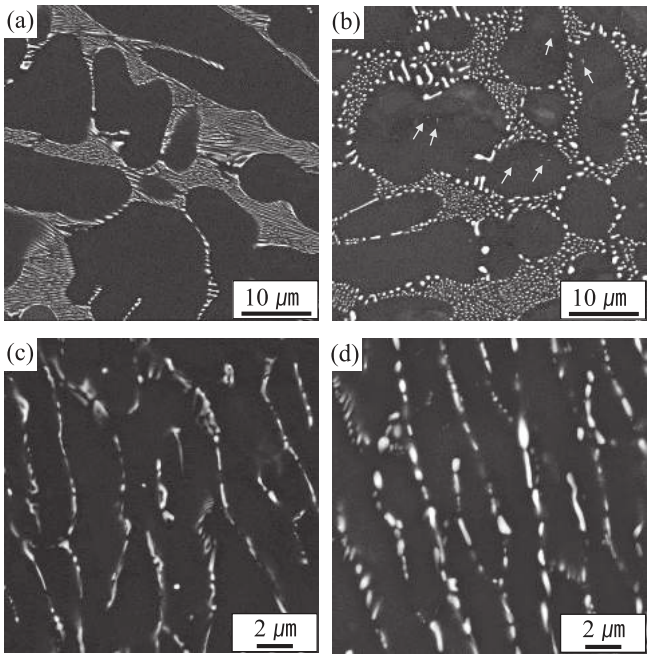

Fig. 6 Back-scattered images of Al-Mn-Fe alloy. (a) as-cast DC-cast, (b) as-HOMO DC-cast, (c) as-cast HSTRC strip, (d) as-HOMO HSTRC strip.

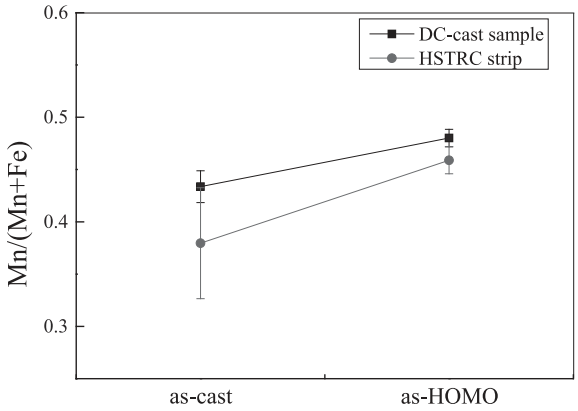

Fig. 7 Mn/(Mn+Fe) composition ratio change of constituent particles in Al-Mn-Fe alloy for DC-cast sample and HSTRC strip.

spheroidization and coarsening of constituent $Al_6(Mn,Fe)$ phase during HOMO at similar temperature range is also observed in other Al-Mn based alloys[23,24]. During the heat treatment, the decomposition of supersaturated Mn element appears in a range from 300 to 600°C by the formation of new dispersoids and coarsening of primary particles. Simultaneously, re-dissolution of fine second-phase particle can also occur. These formation of new dispersoids and coarsening of primary particles, and dissolution of fine particles are competitive processes for decomposition of the solid solution. In the present study, around 0.27 mass% Mn solute element was decomposed during HOMO in DC-cast sample (see Table 2). It is hard to assume that the decomposition of the solid solution is mainly controlled by precipitation because of less amount of new dispersoids formation (Fig. 6 (b)). Also, the applied HOMO temperature in this study is lower than the re-dissolution temperature of primary $Al_6(Mn,Fe)$ phase. Thus, it can be assumed that the decomposition of supersaturated Mn in solid solution is correlated with constituent particle coarsening. Figure 7 shows Mn/(Mn+Fe) compositional ratio change in constituent particle for DC-cast and HSTRC strip during HOMO. In as-cast condition, constituent particles had relatively lower Mn/(Mn+Fe) ratio, while the Mn/(Mn+Fe) ratio increased after HOMO. This is because the supersaturated Mn diffuses into the constituent $Al_6(Mn,Fe)$ phase. Diffusion of Mn into the particles can lead to particle growth and coarsening. The continuous change in chemical compositions of constituent $Al_6(Mn,Fe)$ phase was also reported[23,25]. In HSTRC strip, more amount of decomposition of supersaturated Mn content was observed after HOMO compared to DC-cast in spite of equivalent value of Mn supersaturation level in as-cast condition. The HSTRC strip indicated much finer primary α-Al dendrite and homogeneously disbributed constituent particles in as-cast condition due to its high cooling rate as shown in Fig. 6 (c). Therefore, it can be assumed that the diffusion of supersaturated Mn in α-Al dendrite to constituent particles is easy to occur because the relevant diffusion length is short in HSTRC strip. For this reason, HSTRC strip showed much amount of decomposition of supersaturated Mn content during HOMO. Additionally, it is also possible the more amount of precipitation of new dispersoids in HSTRC during HOMO resulting from relatively homogeneous Mn solute distribution in Al matrix due to its high cooling rate during solidification.

3.4.2 Al-Mn-Si ternary alloy

Figure 8 shows the EPMA results of AMS for DC-cast and HSTRC strip as-cast condition. The area subjected for EPMA analysis was marked by dotted line as shown in Fig. 8 (a) and (b). From the solute distribution state in DC-cast sample, it can be seen that the Mn concentration in matrix (Fig. 8 (c)) increased from the center to the periphery of α-Al dendrite. In the present study, the Mn element mapping result reflects the influence by not only supersaturated Mn in Al matrix but also the Mn containing constituent particles. So, high Mn composition in the interdendritic region is the influence of constituent particles. There are some regions displayed in black at the interdendritic region. It is considered the place where the constituent particle detached during sample preperation such as polishing. In Si element mapping, the solute distribution was more clearly revealed than that of Mn element. The Si content was low inside of α-Al dendrite cells as shown in Fig. 8 (d). Note that this inhomogeneous solute distribution is well corresponded to the dispersoids distribution after HOMO as shown in Fig. 4 (b). Meanwhile, HSTRC with high cooling rate showed relatively higher solute concentration in Al matrix. Also, homogeneous solute distribution in Al matrix was clearly observed in Si as well as Mn element. It is due to the high cooling rate of HSTRC during solidification. This difference of solute distribution in Al matrix on DC-cast sample and HSTRC strip can affect the formation of dispersoids and its distribution after HOMO.

Figure 9 shows the back-scattered images of AMS alloy DC-cast and HSTRC strip, respectively. For DC-cast sample, it can be seen that the constituent particles were observed at the grain boundaries and within the grain, where

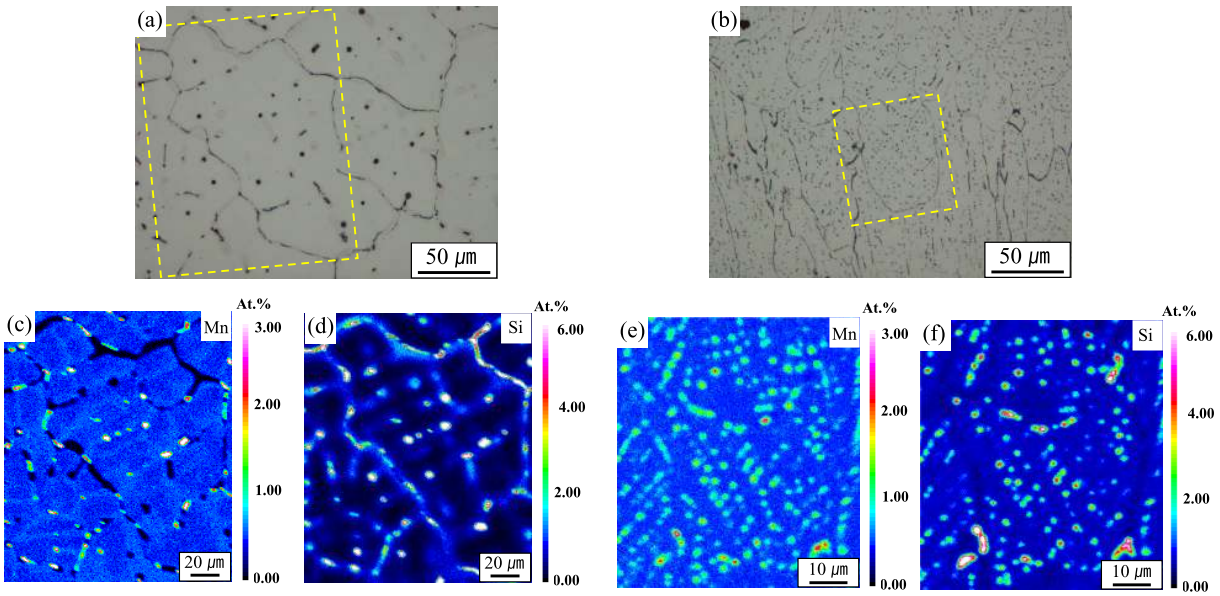

Fig. 8 Solute distribution in Al-Mn-Si alloy. Locations where the EPMA analysis was performed in (a) DC-cast, and (b) HSTRC strip. Element mapping results of (c) Mn in DC-cast, (d) Si in DC-cast, (e) Mn in HSTRC strip, (f) Si in HSTRC strip.

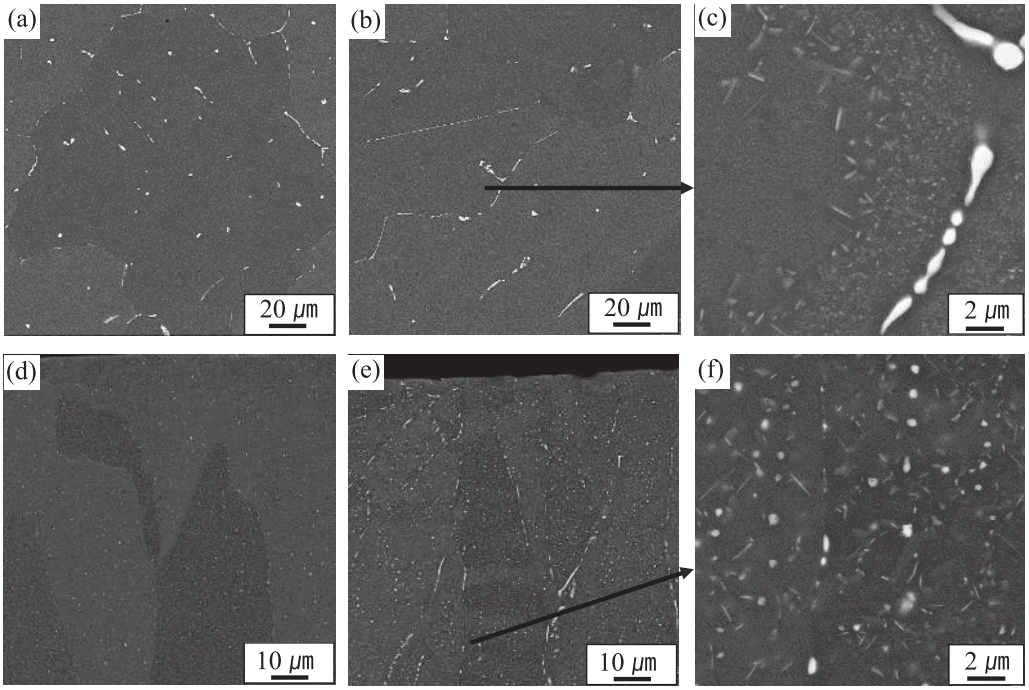

Fig. 9 Back-scattered images of Al-Mn-Si alloy. (a) as-cast DC-cast, (b) as-HOMO DC-cast, (c) detail of specific area in (b), (d) as-cast HSTRC strip, (e) as-HOMO HSTRC strip, (f) detail of specific area in (e).

the final solidification of the solute-enriched liquid occurred (Fig. 9 (a)). After HOMO, fine dispersoids were observed on the periphery of α-Al dendrite, and dispersoids-free area was observed at the core of α-Al dendrite as shown in Fig. 9 (b) and (c). It is corresponded to the solute distrubiton in Al matrix, particularly Si element. For HSTRC strip, much finer and well distributed constituent particles were observed in as-cast condition (Fig. 9 (d)). In as-HOMO condition, fine dispersoids were homogeneously distributed inside of grains as shown in Fig. 9 (e) and (f). It is also well coincided with the solute distribution of Si as well as Mn. In Al-Mn-Si ternary alloy, the formation of new dispersoids mainly controls decomposition of supersaturated Mn in solid solution, which is correlated with the diffusion of Si element. It is known the Si element diffuses from the matrix into the particles during heat treatment, then constituent particles such as Al_6(Mn,Fe) transforms to cubic α-Al(Mn,Fe)Si phase[26,27]. For AMS in the present study, there was less Al_6(Mn,Fe) phase as constituents because of less Fe contents. So, the Si element in Al matrix was not be spent for transformation from Al_6(Mn,Fe) to α-Al(Mn,Fe)Si during HOMO. Instead, most of Si element constributes to decompose the supersaturated

Mn in solid solution as formation of α-AlMnSi phase. As shown in Fig. 8 (c) and (d), the solute distribution was inhomogeneous in DC-cast sample, especially Si element. Since the lack of solute Si concentration inside of α-Al dendrite in DC-cast sample, formation of dispersoids is hard to occur as shown in Fig. 9 (c). In contrast, HSTRC strip showed homogeneous solute distribution in Si as well as Mn element due to its high cooling rate during solidification. This solute distribution can promote the Mn-containing dispersoids precipitation in extensive range. For this reason, homogeneous solute distribution of Si as well as Mn in HSTRC strip results in much amount of decomposition of supersaturated Mn in solid solution by formation of high-dense dispersoids.

4. Conclusion

In order to investigate the effect of cooling rate on the solute distribution in Al matrix, Al-Mn based alloys were fabricated by high-speed twin-roll casting and DC-casting with different cooling rates. The solute distribution during solidification played an important role in the evolution of dispersodis after HOMO. The results of the analyses are summarized as follows:

(1) From the temperature profile of HSTRC obtained by direct measurement, the average cooling rate was estimated over 10^3 K/s in HSTRC strip center as well as surface area. It contributes to not only the refinement of primary α-Al dendrite and constituent particle size but also homogenoeus distribution of solute elements in Al matrix.

(2) The Mn solid solubility was estimated from the electrical conductivity change. The level of Mn concentration was equivalent in as-cast condition in spite of different cooling rate during solidification. However, amount of decomposed Mn content was different after homogenization. This was dependent on the distribution of constituent particle and solute distribution in Al matrix.

(3) In binary Al-Mn alloy, decomposition of Mn content in solid solution was not observed after homogenization. It was confirmed that alloying elements such as Fe and Si have significant role to decompose Mn content in solid solution.

(4) Fine constituent particle and its homogeneous distribution were observed in HSTRC strip resulting from high cooling rate during solidification. Decomposition of supersaturated Mn in solid solution resulted in the coarsening of the constituent particles during homogenization.

(5) Formation of fine dispersoids was predominantly observed in Al-Mn-Si alloy. Decomposition of supersaturated Mn was strongly dependent on the solute distribution in Al matrix especially Si element. Due to high cooling rate, HSTRC strip showed high concentration and homogeneous Mn and Si distribution in Al matrix. This contributes to enhance decomposition of supersaturated Mn in solid solution during homogenization.

Acknowledgments

The authors acknowledge for the financial support from the Japan Foundry Engineering Society.

REFERENCES

1) F.J. Humphreys and M. Hatherly: *Recrystallization and Related Annealing Phenomena: Second Edition*, (Elsevier, Oxford, 2004) pp. 285–319.
2) R.D. Doherty, D.A. Hughes, F.J. Humphreys, J.J. Jonas, D. Juul Jensen, M.E. Kassner, W.E. King, T.R. McNelley, H.J. McQueen and A.D. Rollett: Mater. Sci. Eng. A **238** (1997) 219–274.
3) F.J. Humphreys: Acta Metall. **25** (1977) 1323–1344.
4) F.J. Humphreys and P.N. Kalu: Acta Metall. **35** (1987) 2815–2829.
5) K. Huang, O. Engler, Y.J. Li and K. Marthinsen: Mater. Sci. Eng. A **628** (2015) 216–229.
6) M. Karlík, T. Mánik and H. Lauschmann: J. Alloy. Compd. **515** (2012) 108–113.
7) Y.J. Li, A.M.F. Muggerud, A. Olsen and T. Furu: Acta Mater. **60** (2012) 1004–1014.
8) A.M.F. Muggerud, E.A. Mørtsell, Y.J. Li and R. Holmestad: Mater. Sci. Eng. A **567** (2013) 21–28.
9) T. Haga, K. Tkahashi, M. Ikawaand and H. Watari: J. Mater. Process. Technol. **153–154** (2004) 42–47.
10) K. Suzuki, S. Kumai, Y. Saito, A. Sato and T. Haga: Mater. Trans. **45** (2004) 403–406.
11) S. Kumai, K. Kobayashi, H. Zhu, K. Suzuki and T. Haga: JJILM **55** (2005) 500–506.
12) K. Suzuki, S. Kumai, Y. Saito and T. Haga: Mater. Trans. **46** (2005) 2602–2608.
13) M.S. Kim, Y. Arai, Y. Hori and S. Kumai: Mater. Trans. **51** (2010) 1854–1860.
14) M.S. Kim and S. Kumai: Mater. Trans. **52** (2011) 856–861.
15) D. Shimosaka, S. Kumai, F. Casarotto and S. Watanabe: Mater. Trans. **52** (2011) 920–927.
16) M.S. Kim and S. Kumai: Mater. Trans. **54** (2013) 1930–1937.
17) J.E. Hatch: *Aluminum; Properties and Physical Metallurgy*, (1984) pp. 204–206.
18) L.A. Willey: *Aluminum*, Vol.1, ASM (1967) p. 359.
19) S. Komatsu and S. Fujikawa: JJILM **47** (1997) 170–181.
20) P. Kolby, C. Sigli and C.J. Simensen: *Aluminum Alloys: Their Physical and Mechanical Properties*, ICAA4, Atlanta, USA, (1994) pp. 508–512.
21) P.C.M. De Haan, J. Van Rijkom and J.A.H. Söntgerath: Mater. Sci. Forum **217** (1996) 765–770.
22) Y.J. Li and L. Arnberg: Acta Mater. **51** (2003) 3415–28.
23) Y.J. Li and L. Arnberg: Mater. Sci. Eng. A **347** (2003) 130–135.
24) K. Liu and X.G. Chen: Mater. Des. **84** (2015) 340–350.
25) M. Dehmas, E. Aeby-Gautier, P. Archambault and M. Serrière: Metall. Mater. Trans., A **44** (2013) 1059–1073.
26) D.T.L. Alexander and A.L. Greer: Acta Mater. **50** (2002) 2571–2583.
27) E. Trømborg, A.L. Dons and L. Arnberg: *Aluminium Alloys: Their Physical and Mechanical Properties*, ICAA3, Trondheimin, SINTEF Metallurgy, (1992) pp. 270–275.